Hindawi Publishing Corporation
EURASIP Journal on Wireless Communications and Networking
Volume 2007, Article ID 57980, 16 pages
doi:10.1155/2007/57980

Research Article

Polarization Behavior of Discrete Multipath and Diffuse Scattering in Urban Environments at 4.5 GHz

Markus Landmann,[1] Kriangsak Sivasondhivat,[2] Jun-Ichi Takada,[2] Ichirou Ida,[3] and Reiner Thomä[1]

[1] *Electronic Measurment Research Lab, Institute of Information Technology, Ilmenau University of Technology, P.O. Box 100 565, 98684 Ilmenau, Germany*
[2] *Department of International Development Engineering, Takada Laboratory, Graduate School of Engineering, Tokyo Institute of Technology, Tokyo 152-8552, Japan*
[3] *Fujitsu Limited, Tokyo 105-7123, Japan*

Received 13 April 2006; Revised 7 November 2006; Accepted 15 November 2006

Recommended by Rodney A. Kennedy

The polarization behavior of the mobile MIMO radio channel is analyzed from polarimetric double-directional channel measurements, which were performed in a macrocell rural environment in Tokyo. The recorded data comprise non-line-of-sight, obstructed line-of-sight, and line-of-sight conditions. The gradient-based maximum-likelihood estimation framework RIMAX was used to estimate both specular and dense multipath components. Joint angular-delay results are gained only for the specular components. The dense multipath components, which may be attributed to diffuse scattering, can be characterized only in delay domain. Different characteristics describing the polarization behavior and power-weighted cross- and copolarization ratios for both types of components are introduced. Statistical analysis of long measurement track segments indicates global trends, whereas local analysis emphasizes specific behavior such as polarization dependency on angle of incidence in streets and under shadowing conditions. The results also underline the importance of modeling changing and transient propagation scenarios which are currently not common in available MIMO channel models.

1. INTRODUCTION

Efficient design of MIMO transmission systems requires a thorough understanding of the multidimensional structure of the mobile radio channel. Initially, research was aimed at the spatiotemporal channel structure at base-station side only. The appearance of MIMO systems forced a more detailed description of the mobile radio channel at both transmitter and receiver sides including directions of arrival and departure. Recent simulations [1, 2] and measurements [3–6] showed that the capacity of MIMO systems can be further enhanced if the polarimetric dimension is exploited. Moreover, dual polarimetric antennas can be colocated (e.g., patch antennas), which is a space- and cost-effective alternative to two spatially separated antennas with the same polarization. The draw back of the existing results (as mentioned above) is to consider the antennas as a part of the radio channel. There was no attempt to separate the channel characteristics from antennas influence in both the measurement and simulation cases.

The aim of our work is measurement-based parametric channel modeling (MBPCM) [7]. The idea behind this method is to deduce a parametric model of the MIMO channel that is (within well-defined limits) independent from the antennas used during the measurement. This offers the possibility to emulate the MIMO transfer properties of arbitrary antenna arrays (again within well-defined limits) by reconstructing the hypothetical antenna response from the estimated channel parameters. The key technologies to estimate the individual path parameters, removed from the antenna influence, are high-resolution parameter estimation [8–10] and precise antenna calibration [11]. There are only a few dual polarized and double-directional channel measurements described in the literature where these algorithms are applied and the estimated parameters are analyzed (see [12] MIMO), (see [13, 14] SIMO). We are using the gradient-based maximum-likelihood estimation framework RIMAX

[10] that estimates both specular and dense multipath components. However, joint angular-delay results are gained only for the specular components. The dense multipath components, which may be attributed to diffuse scattering, can be characterized only in delay domain. We present statistical analysis of sets of segments that indicate global trends, whereas local analysis emphasizes specific behavior such as polarization on angle of incidence in streets and under shadowing conditions. The results underline the importance of modeling of evolving and transient propagation scenarios, which is currently not common in available MIMO channel models. This supports the current discussions in propagation modeling community [15, 16], which indicates also a deficiency in modelling of polarization.

The paper is organized as follows: Section 2 gives a brief review of the RIMAX parameter estimation framework. In Section 3, we present the sounder and data processing system that were used throughout the measurement campaign. An overview on the propagation environment and a first general classification of the estimated results are given in Section 4. Section 5 discusses the different parameters and their definitions describing the polarization behavior of the channel. In Section 6, the statistical analysis along sets of segments of the measurement run and local analysis results are discussed. Finally, local results with specific behavior are pinpointed.

2. CHANNEL CHARACTERIZATION

In case of the experimental channel characterization, antennas or antenna arrays at the BS and MS are part of the measured links. Since we want to characterize the channel independent from the used antenna arrays, high-resolution parameter estimation algorithms are applied to the measurement data. In our contribution, we use the gradient-based maximum-likelihood parameter estimation algorithm RIMAX [10, 17]. The appropriate data model comprises two components which can be handled separately throughout the estimation procedure. The first part is deterministic and results from specular-like reflection. Each specular component (SC) k is characterized by its parameters direction of departure (DoD) $\varphi_{\mathrm{T}k}$, $\vartheta_{\mathrm{T}k}$ (azimuth and elevation), time delay of arrival (TDoA) τ_k, Doppler shift α_k, direction of arrival (DoA) $\varphi_{\mathrm{R}k}$, $\vartheta_{\mathrm{R}k}$, and the four complex polarimetric path weights $\gamma_{\mathrm{hh},k}$, $\gamma_{\mathrm{hv},k}$, $\gamma_{\mathrm{vv},k}$, $\gamma_{\mathrm{vh},k}$, where the first subscript indicates the polarization at the BS side and the second at the MS side (Figure 1(b)). The vector of the vertical (v) polarization is parallel to the vector $\vec{e}_\theta$ and the vector of the horizontal (h) polarization is parallel to the vector $\vec{e}_\phi$ of the spherical coordinate system. Furthermore, the RIMAX calculates the variances $\sigma_{\varphi_{\mathrm{T}k}}$, $\sigma_{\vartheta_{\mathrm{T}k}}$, σ_{τ_k}, σ_{α_k}, $\sigma_{\varphi_{\mathrm{R}k}}$, $\sigma_{\vartheta_{\mathrm{R}k}}$, $\sigma_{\Re\{\gamma_{\mathrm{hh},k}\}}$, $\sigma_{\Im\{\gamma_{\mathrm{hh},k}\}}$, $\sigma_{\Re\{\gamma_{\mathrm{vv},k}\}}$, $\sigma_{\Im\{\gamma_{\mathrm{vv},k}\}}$, $\sigma_{\Re\{\gamma_{\mathrm{hv},k}\}}$, $\sigma_{\Im\{\gamma_{\mathrm{hv},k}\}}$, $\sigma_{\Re\{\gamma_{\mathrm{vh},k}\}}$, and $\sigma_{\Im\{\gamma_{\mathrm{vh},k}\}}$ of each path based on the Fischer information matrix [10]. Hereby, the estimated variances are used to verify the estimation results of the kth path. The relative variances of the path weights are calculated, where a path with a relative variance better than -3 dB is considered as reliable and paths with a worse relative variance are dropped. This threshold is reasonable since a relative variance of -3 dB stands for equal signal power and noise power. In case of the SCs, the complex polarimetric pathweights are independent from the used measurement antennas, that is, since we estimate the DoD and DoA, we are able to exclude the effect of the polarimetric antenna beam patterns.

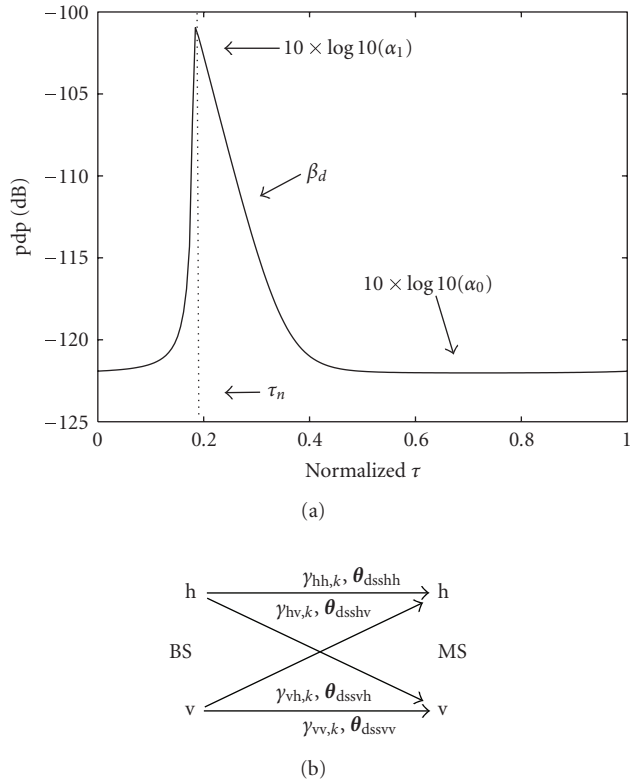

Figure 1: Model of the DMC (a), SC polarization and DMC polarization schematic (b).

The second part of the data model represents the dense multipath components (DMC) that mainly result from distributed diffuse scattering. The DMCs are considered as the remaining complex impulse responses after removing the contribution of the reliable estimated SCs and measurement noise. As an extension to the estimation process in [17], the distribution of the DMC,

$$\alpha(\tau) = \begin{cases} \alpha_0, & \tau < \tau_n, \\ \dfrac{1}{2}\alpha_1, & \tau = \tau_n, \\ \alpha_0 + \alpha_1 \cdot \mathrm{e}^{-\beta_{\mathrm{d}} \cdot (\tau - \tau_n)}, & \tau > \tau_n, \end{cases} \tag{1}$$

shown in Figure 1(a) is estimated independently for all four polarization combinations from the corresponding mean power delay profile (PDP). In the following, we describe the calculation of these four PDPs. The subtraction of the specular components from the vector-valued measured impulse responses $\mathbf{h}_{i,xy}$ leads to the remaining complex impulse responses $\mathbf{h}'_{i,xy}$ of all i, xy channels, where x specifies the port polarization at BS side, y specifies the port polarization at the

Table 1: Measurement system.

MIMO channel sounder	RUSK Fujitsu [18]
Tx power at the antenna	ca 2.8 W
Carrier frequency/wavelength	4.5 GHz/λ = 6.67 cm
Measurement bandwidth	120 MHz
Maximum multipath delay	3.2 μs chosen according to the environment
Number of multiplexed Tx/Rx ports	16 Tx/96 Rx
Total number of MIMO channels	1536
Measurement time of one snapshot	10 milliseconds
Time between 2 snapshots	1.5 seconds
Tx/Rx synchronization	Rubidium reference
Base station (Tx side)	4-by-2 element polarimetric uniform rectangular patch array (PURPA)
Mobile station (Rx side)	24-by-2 element stacked polarimetric uniform circular patch array (SPUCPA)
XPD [19, equation (13)] Tx/Rx array	13 dB, . . . , 15 dB/10 dB, . . . , 14 dB

MS, side and i indicates one channel of all available channels I with the polarization combination xy. Each port of the antenna array has been designated either as horizontal or vertical. Consequently, x and y are either h or v. To compensate the effect of the antenna beam patterns at least partly (as no directional information is considered) for the DMC, $\mathbf{h}'_{i,xy}$ is divided by the *mean* gains $g_{i,x}$ and $g_{i,y}$ (3) of the corresponding Tx and Rx port,

$$\mathbf{h}''_{i,xy} = \frac{\mathbf{h}'_{i,xy}}{\sqrt{g_{i,x} \cdot g_{i,y}}}. \tag{2}$$

The mean gain

$$g_{i,q} = \frac{1}{S} \cdot \sum_{n=n_1}^{n_2} \sum_{m=m_1}^{m_2} \left| b_{i,q}(n \cdot \Delta\varphi, m \cdot \Delta\vartheta) \right|^2 \cdot \sin(m \cdot \Delta\vartheta) \tag{3}$$

is calculated from the measured beam pattern $b_{i,q}(\varphi, \vartheta)$ for polarization q, where q is chosen equal to the port polarization x or y. This means that the cross-polarization term of the port is neglected. The indices n_1, n_2 and m_1, m_2 specify the azimuth and coelevation ranges, and $S = N \cdot M$ the total number of samples that are used for the calculation of the mean gain with $N = n_2 - n_1 + 1$ and $M = m_2 - m_1 + 1$. Using this approach, the assumption has been made that the DMCs are uniformly distributed in the chosen azimuth and coelevation ranges. In our analysis, we observed that after removing the contribution of the specular propagation paths from the measured complex impulse responses the, power delay-azimuth profile of the remaining complex impulse responses has only a few directional information in the MS azimuth (similar observations were found in [20]). Therefore, the ranges at the MS side are chosen between 45° to 135° in coelevation with respect to the surrounding area and between −180° to 180° in azimuth. At the BS side, it was found that it is reasonable to limit the range to the broadside direction, where the azimuth range is chosen between −70° to 70° and the coelevation range between 80° to 140°. The values $\Delta\varphi$, $\Delta\vartheta$ are the corresponding step sizes in azimuth and coelevation that are chosen to (1°).

The four parameter vectors of the DMCs $\boldsymbol{\theta}_{\text{dsshh}}$, $\boldsymbol{\theta}_{\text{dsshv}}$, $\boldsymbol{\theta}_{\text{dssvh}}$, and $\boldsymbol{\theta}_{\text{dssvv}}$ (Figure 1(b)), composed of the parameters $\boldsymbol{\theta}_{\text{dss}xy} = [\alpha_{0,xy}, \alpha_{1,xy}, \beta_{\text{d},xy}, \tau_{\text{n},xy}]$, are estimated from the mean PDP $\boldsymbol{\rho}_{xy}$,

$$\boldsymbol{\rho}_{xy} = \frac{1}{I} \sum_{i=1}^{I} \left| \mathbf{h}''_{i,xy} \right|^2 \tag{4}$$

of the corresponding polarization combination xy.

3. MEASUREMENT TECHNIQUE AND DATA PROCESSING

The configuration of the measurement system is summarized in Table 1. We used well-calibrated antenna arrays (manufactured by IRK Dresden [21]) at both link ends, which allow us to estimate the cross-polarization ratio (XPR) of the SCs up to ±40 dB. This limitation is caused by the usage of a reference horn antenna with a cross-polarization discrimination (XPD) of 40 dB during the calibration of the Rx and Tx antenna arrays. For the DMCs, the maximum resolvable XPR of the channel is limited by the XPD of the antenna array elements, given in Table 1. Note that the XPD is a property of the antenna element, whereas the XPR describes the polarization behavior of the channel.

Table 2: Measurement environment.

Environment	macrocell
BS (Tx) height	35 m
MS (Rx) height	1.6 m
Building heights around Rx	2-3 floors, mostly residential area
Total measurement route	490 m (ca 2000 snapshots)
Number of measured segments	45 (see Figure 2)

For the purpose of the offline measurement data processing, by using the RIMAX algorithm, ca 10 PCs are organized in a batch processing system. To process the total amount of measurement data, the system was continuously running for 3 weeks.

4. MEASUREMENT DESCRIPTION AND ENVIRONMENT CHARACTERIZATION

In Section 4.1, we give a description of how and where the measurements were performed. Additionally, background information is presented on the total power of the estimated SCs and their path length spread at each measurement position (Section 4.2).

4.1. General description

The measurements were performed in a macrocell environment. Table 2 summarizes the basic information of the scenario. The same system setup and measurement procedure are applied during the entire campaign, where we used only one BS (Tx) position while moving to different MS (Rx) positions. The measurement route is divided in segments of 10 meters. In Figure 2, the significant positions like corners are labeled with crosses. Each segment is measured in the same way: 10 static snapshots at the start position, ca 40 snapshots while moving to the next position (i.e., an approximate speed of 25 cm/snapshot), 10 static snapshots at the end. The measurements are carried out in the neighborhood of Minami-Senzoku, Ota-Ku, Tokyo (Figure 3), where the transmit antenna array (BS) is placed over roof top at a 10-floor high building in the nearby campus of the Tokyo Institute of Technology. The receive antenna array (MS) is placed at a cart around 1.6 m above the street, where the buildings in the surrounding residential area are between two and three flours high.

4.2. Environment characterization

The data model used comprises the two components SC and DMC. For an analysis of the results related to these two components, we will indicate the percentage of total power that is estimated as SC. Figure 4 shows the total specular power as a percentage at each point.

(i) In the line-of-sight (LOS) case, moving from position Rx1 to Rx6 (see Figure 2), the total specular power represents around 95% of the signal power.

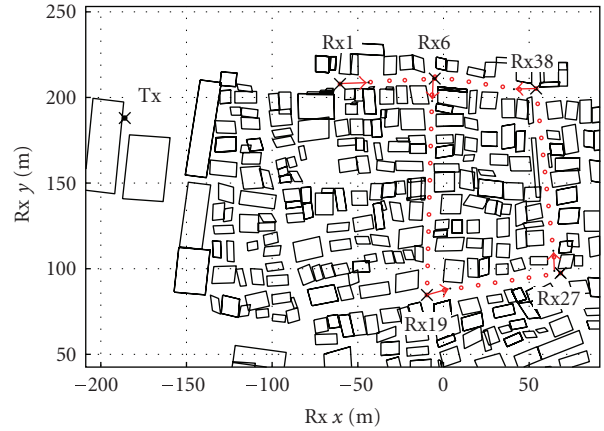

Figure 2: Map of macrocell measurement site.

Figure 3: Picture taken from Tx in the direction of Rx6 macrocell.

(ii) The measurements between position Rx6 and Rx19 are mostly non-line-of-sight (NLOS) with a total SC power of around 55% to 65%. However, at some positions, the specular power increases to up to 80%, which is mainly caused by strong single bounce scattering and obstructed line of sight (OLOS). In the parallel street between positions Rx27 and Rx38, we observe similar behavior.

(iii) In the street between position Rx19 and Rx27, the portion of SCs is almost constant (around 55%). All measurements here were taken under NLOS conditions. Furthermore, strong single bounce reflections and OLOS are rare.

(iv) The measurements between Rx38 and Rx6 are dominated by strong single-bounce scattering and OLOS around the corner of Rx6. The total SC power is between 65% to 85%.

Plotting the CDF of the specular power for all measurements (Figure 5), it is apparent that a strong relation exists between the conditions LOS, OLOS, NLOS, and this parameter.

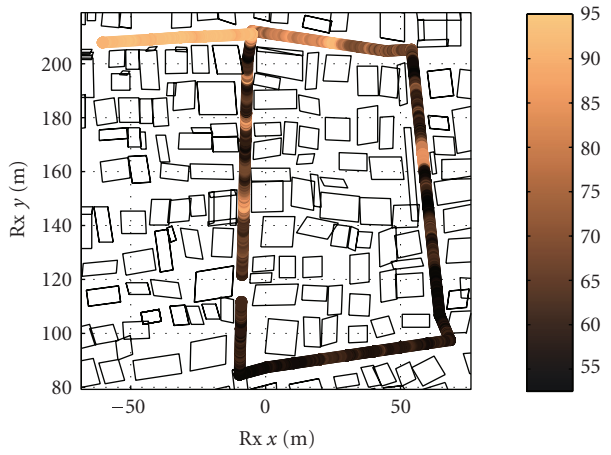

FIGURE 4: Specular power macrocell color-coded in %.

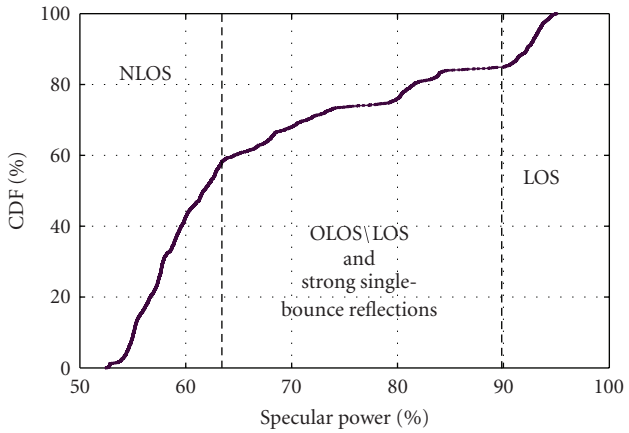

FIGURE 5: CDF of the specular power of the entire route.

To distinguish between local scattering around Rx and far scattering, the path length spread of the SCs and DMCs is discussed, which is equivalent to the estimated delay spread multiplied by the speed of light. Figure 6 shows the path length spread at each position. It is noted that these values increase drastically around corner Rx19. The causes for that behavior are some far clusters, of which 2 clusters are indicated by arrows in Figure 6. All other regions are dominated by local scattering.

The far clusters were localized on basis of estimated angles of the SCs at the BS and MS sides (see Figure 7). Each path is plotted with half of the path length from Tx and Rx in the scenario. The colors indicate the total power of a path in dB. In Figure 8, the CDFs of the path length spread of the SCs and DMCs are compared. The path length spread of the DMCs is calculated from the parameter β_d, which corresponds to the coherency bandwidth and which is inversely proportional to the delay spread. For the DMC, a smaller variation is observed compared to the SCs. We conclude that the DMC process is mainly influenced by local scattering. The authors abstain from a detailed discussion of the es-

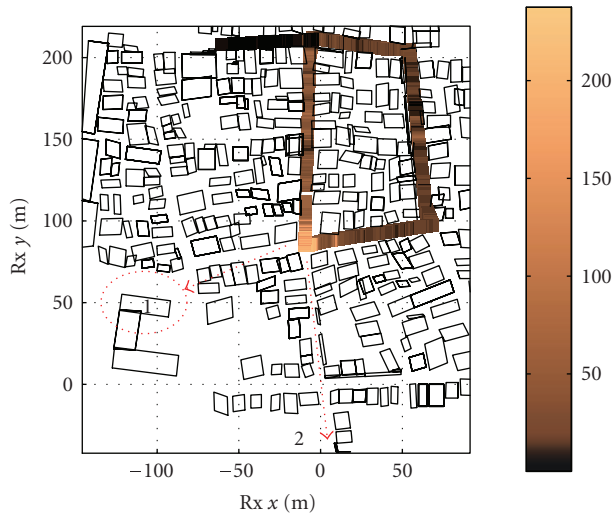

FIGURE 6: Path length variation in m, where the arrows indicate the position of far clusters (no. 2 not on the map).

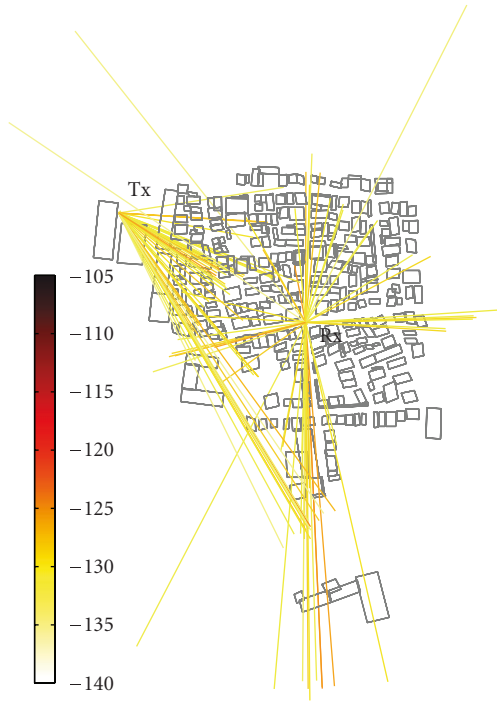

FIGURE 7: DoA, DoD, and TDoA (as length) for all paths at Rx19.

timated angular parameters and far clusters (can be found in [22]). The angular parameters are used in Section 6.3 to identify the cause of specific channel characteristics.

5. HOW TO DEFINE THE POLARIZATION BEHAVIOR OF THE CHANNEL

A lot of publications on XPR exist, but different definitions were found. With the following discussion, the authors

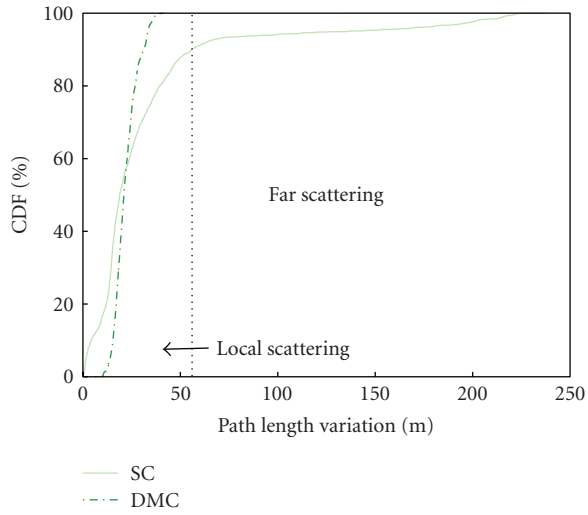

Figure 8: CDF of the path length variation.

would like to point out the difficulties of a comparison of various published results. The XPR is basically defined as the power ratio between the copolarization and the cross-polarization. In [23], the power ratio between P_{qq} and P_{qp} at the MS side, respectively, P_{pq} at the BS side,

$$\begin{aligned} \mathrm{XPR}_q^{\mathrm{MS}} &= 10 \cdot \log_{10}\left(\frac{P_{qq}}{P_{qp}}\right)(\mathrm{dB}), \\ \mathrm{XPR}_q^{\mathrm{BS}} &= 10 \cdot \log_{10}\left(\frac{P_{qq}}{P_{pq}}\right)(\mathrm{dB}), \end{aligned} \tag{5}$$

is used, where q and p can be either horizontal or vertical. To calculate the powers P_{qq}, P_{qp}, or P_{pq}, the powers of all qq, qp or pq channels are added up, for example,

$$P_{qq} = \sum_{i=1}^{I} \left| \mathbf{h}_{i,qq}^{\mathrm{H}} \cdot \mathbf{h}_{i,qq} \right|, \tag{6}$$

whereas the column vector $\mathbf{h}_{i,qq}$ is the ith complex impulse response with the polarization qq. Using this definition, a reliable estimated XPR is limited to the XPD of the single-antenna elements.

Another approach uses beam forming or high-resolution parameter estimation to detect individual rays/paths. Here, two definitions can be found, the XPR of a single path k [13]:

$$\begin{aligned} \mathrm{XPR}_{q,k}^{\mathrm{MS}}(s) &= 10 \cdot \log_{10}\left(\left|\frac{\gamma_{qq,k}(s)}{\gamma_{qp,k}(s)}\right|^2\right)(\mathrm{dB}), \\ \mathrm{XPR}_{q,k}^{\mathrm{BS}}(s) &= 10 \cdot \log_{10}\left(\left|\frac{\gamma_{qq,k}(s)}{\gamma_{pq,k}(s)}\right|^2\right)(\mathrm{dB}), \end{aligned} \tag{7}$$

where s is the snapshot index, and the narrowband XPR of the L_c paths of a cluster c [24]:

$$\mathrm{XPR}_{q,c}^{\mathrm{MS}}(s) = 10 \cdot \log_{10}\left(\left|\frac{\sum_{n=1}^{L_c} \gamma_{qq,n,c}(s)}{\sum_{n=1}^{L_c} \gamma_{qp,n,c}(s)}\right|^2\right)(\mathrm{dB}). \tag{8}$$

Using these definitions, a reliable estimation of the XPR of a cluster or the SCs is limited to the XPD of the reference horn antenna during the antenna array calibration (see Section 3) in the case of double-directional measurements. This is in contrast to, for instance, single-directional measurements. Due to the fact that a single Tx antenna is used, the angle-of departure cannot be resolved, so compensation for angle dependent XPD is not possible. As a result, a reliable estimation of the XPR is limited to the XPD of the transmit antenna, which normally varies between 8 dB and 20 dB depending on the direction of departure.

In the following, we define the parameters which are used during the analysis (Section 6) illustrated with examples from the measurement segments Rx19 to Rx27. The basic parameters are defined for both, the BS and MS sides, whereas the distributions are only shown for the MS parameters. In Section 5.1, the XPR distribution based on (7) for SCs and DMCs are discussed, whereas in Section 5.2 the power-weighted XPR is defined.

5.1. XPR distribution

Definition (7) describes how a single propagation path has to be modeled in terms of the XPR regardless of the importance of the path in terms of its total received power.

Figures 11 and 12 show the PDFs of the $\mathrm{XPR}_{\mathrm{h}}^{\mathrm{MS}}$ and $\mathrm{XPR}_{\mathrm{v}}^{\mathrm{MS}}$ of the SCs for the chosen measurement segment Rx19 to Rx27. The best fit to the normal distribution is plotted in the PDF of the measurement. The expectation and standard deviation of the measurement agree with those of the fitted distribution. This agreement can be observed also for the other segments (not shown).

For a better understanding of the polarization behavior, we analyze the copolarization ratio or the ratio of the total received or transmitted vertical power to the horizontal power $P_{\mathrm{v/h}}^{\mathrm{MS}}$ or $P_{\mathrm{v/h}}^{\mathrm{BS}}$ (9) (Figure 13) as well:

$$\begin{aligned} P_{\mathrm{v/h},k}^{\mathrm{MS}}(s) &= 10 \cdot \log_{10}\left(\frac{\left|\gamma_{\mathrm{vv},k}(s)\right|^2 + \left|\gamma_{\mathrm{hv},k}(s)\right|^2}{\left|\gamma_{\mathrm{hh},k}(s)\right|^2 + \left|\gamma_{\mathrm{vh},k}(s)\right|^2}\right)(\mathrm{dB}), \\ P_{\mathrm{v/h},k}^{\mathrm{BS}}(s) &= 10 \cdot \log_{10}\left(\frac{\left|\gamma_{\mathrm{vv},k}(s)\right|^2 + \left|\gamma_{\mathrm{vh},k}(s)\right|^2}{\left|\gamma_{\mathrm{hh},k}(s)\right|^2 + \left|\gamma_{\mathrm{hv},k}(s)\right|^2}\right)(\mathrm{dB}). \end{aligned} \tag{9}$$

To describe the polarization behavior of the DMCs, we apply definition (7) like in the case of the SCs. Therefore, we calculate a sampled version of the DMC distribution (cf. (1)) for all four polarization combinations. We use the distance

$$\Delta\tau = \frac{1}{B} \tag{10}$$

between two samples, where B is the measurement bandwidth. To calculate the XPR of the DMC, the samples $k_{\mathrm{DMC}} = 1, \ldots, K_{\mathrm{DMC}}$ ($K_{\mathrm{DMC}} \in \mathbb{N}$) are used. These samples are in the

range of the largest delay spread of the four DMC processes:

$$\frac{\left(\min\left(\boldsymbol{\theta}_{\beta_d}\right)\right)^{-1}}{\Delta\tau} < K_{\mathrm{DMC}} \leq \frac{\Delta\tau + \left(\min\left(\boldsymbol{\theta}_{\beta_d}\right)\right)^{-1}}{\Delta\tau}, \tag{11}$$

where $\boldsymbol{\theta}_{\tau_n}$ and $\boldsymbol{\theta}_{\beta_d}$ are vectors that include the estimates of τ_n and β_d of all four polarization combinations. The first sample in the delay τ is defined by the minimum base delay $\tau_{n\min} = \min(\theta_{\tau_n})$. To use (7) for the DMC,

$$\gamma_{k_{\mathrm{DMC}},xy} = \sqrt{\alpha_{xy}\left(\tau_{n\min} + \left(k_{\mathrm{DMC}} - 1\right)\cdot\Delta\tau\right)} \tag{12}$$

is defined. The calculated XPR of the DMC, using this definition, is only valid for values smaller than the XPD of the antenna. Consequently, this definition is similar to (5). For the chosen measurement segments, Figures 14 and 15 show the PDFs of the $\mathrm{XPR}_{\mathrm{h}}^{\mathrm{MS}}$ and $\mathrm{XPR}_{\mathrm{v}}^{\mathrm{MS}}$ of the DMCs, where Figure 16 shows the ratio of the total received vertical power to the horizontal of the DMCs.

5.2. Power-weighted XPR distribution

Calculating the expectation of the XPRs (7), each path is assumed to have the same importance. Since every wireless system benefits from the received power, it is necessary to make a difference between paths based on their total received power. Therefore, an effective XPR is defined in which the relation between the received path power and the path XPR is considered. For this purpose, we define an XPR centroid XPRC (first-order moment) (15) and XPR spread XPRS (16). We also define a centroid PC (17) and spread PS (18) of the vertical to horizontal power ratio (9) for a snapshot interval Δs, where s_1 is the first snapshot of the considered interval. In order to combine several snapshots, the power of each path has to be normalized to exclude the effect of the free-space attenuation for different distances between Tx and Rx. Here, we normalize with the mean total power

$$\begin{aligned} P_m(s) = \frac{1}{K(s)}\sum_{k=1}^{K(s)} &\left|\gamma_{\mathrm{hh},k}(s)\right|^2 + \left|\gamma_{\mathrm{hv},k}(s)\right|^2 \\ &+ \left|\gamma_{\mathrm{vh},k}(s)\right|^2 + \left|\gamma_{\mathrm{vv},k}(s)\right|^2 \end{aligned} \tag{13}$$

of all paths in one snapshot s, where $K(s)$ is the total number of estimated paths of the snapshot s. Furthermore, we relate $\mathrm{XPR}_{q,k}^{\mathrm{MS}}(s)$ and $\mathrm{XPR}_{q,k}^{\mathrm{BS}}(s)$ to the normalized powers

$$\begin{aligned} P_{q,k}^{\mathrm{MS}}(s) &= \frac{\left(\left|\gamma_{qq,k}(s)\right|^2 + \left|\gamma_{qp,k}(s)\right|^2\right)}{P_m(s)}, \\ P_{q,k}^{\mathrm{BS}}(s) &= \frac{\left(\left|\gamma_{qq,k}(s)\right|^2 + \left|\gamma_{pq,k}(s)\right|^2\right)}{P_m(s)}, \end{aligned} \tag{14}$$

and $P_{\mathrm{v/h},k}^{\mathrm{MS}}$ and $P_{\mathrm{v/h},k}^{\mathrm{BS}}$ to the total normalized power of all 4 polarimetric path weights $P_k(s)$ (19),

$$\mathrm{XPRC}_q^{\mathrm{MS}}(s_1,\Delta s) = \frac{\sum_{s=s_1}^{s_1+\Delta s}\sum_{k=1}^{K(s)}\mathrm{XPR}_{q,k}^{\mathrm{MS}}\cdot P_{q,k}^{\mathrm{MS}}(s)}{\sum_{s=s_1}^{s_1+\Delta s}\sum_{k=1}^{K(s)}P_{q,k}^{\mathrm{MS}}(s)}, \tag{15}$$

$$\mathrm{XPRS}_q^{\mathrm{MS}}(s_1,\Delta s) = \sqrt{\frac{\sum_{s=s_1}^{s_1+\Delta s}\sum_{k=1}^{K(s)}\left[\mathrm{XPR}_{q,k}^{\mathrm{MS}}(s) - \mathrm{XPRC}_q^{\mathrm{MS}}(s_1,\Delta s)\right]^2\cdot P_{q,k}^{\mathrm{MS}}(s)}{\sum_{s=s_1}^{s_1+\Delta s}\sum_{k=1}^{K(s)}\cdot P_{q,k}^{\mathrm{MS}}(s)}}, \tag{16}$$

$$\mathrm{PC}_{\mathrm{v/h}}^{\mathrm{MS}}(s_1,\Delta s) = \frac{\sum_{s=s_1}^{s_1+\Delta s}\sum_{k=1}^{K(s)}P_{\mathrm{v/h},k}^{\mathrm{MS}}\cdot P_k^{\mathrm{MS}}(s)}{\sum_{s=s_1}^{s_1+\Delta s}K(s)}, \tag{17}$$

$$\mathrm{PS}_{\mathrm{v/h}}^{\mathrm{MS}}(s_1,\Delta s) = \sqrt{\frac{\sum_{s=s_1}^{s_1+\Delta s}\sum_{k=1}^{K(s)}\left[P_{\mathrm{v/h},k}^{\mathrm{MS}} - \mathrm{PC}_{\mathrm{v/h}}^{\mathrm{MS}}\right]^2\cdot P_k^{\mathrm{MS}}(s)}{\sum_{s=s_1}^{s_1+\Delta s}K(s)}}, \tag{18}$$

$$P_k^{\mathrm{MS}}(s) = \frac{\left(\left|\gamma_{qq,k}(s)\right|^2 + \left|\gamma_{qp,k}(s)\right|^2 + \left|\gamma_{pq,k}(s)\right|^2 + \left|\gamma_{pp,k}(s)\right|^2\right)}{P_m(s)}. \tag{19}$$

Figures 17 and 18 show the distribution of the total normalized powers P_{th}^{MS} and P_{tv}^{MS} with

$$P_{tq} = \sum_{s=s_1}^{s_1+\Delta s}\sum_{k=1}^{K(s)}P_{q,k}(s) \tag{20}$$

of all paths and snapshots for the chosen measurements dependent on $\mathrm{XPR}_{\mathrm{h}}^{\mathrm{MS}}$ and $\mathrm{XPR}_{\mathrm{v}}^{\mathrm{MS}}$ of the SCs. These distributions do not follow a normal distribution. This is caused by the dependence of the effective or power-weighted XPR on the measurement position. Comparing the distribution of the copolarization ratio in Figure 13 and the power distribution of the copolarization ratio in Figure 19, we observe similar expectation values and standard deviations. However, the power distribution of the co-polarization does not follow a normal distribution basically due to the local differences in the chosen measurement segment. For this reason, in Section 6, the XPRC and XPRS values will be presented both for sets of segments of the route and for much smaller run lengths Δs.

6. RESULTS

In this section, we will present the results from a stochastical channel model point of view in Section 6.1 and from that of a site-specific model (Sections 6.2 and 6.3).

6.1. Statistical analysis

The parameters XPRC and XPRS of the SCs in Table 3 and the DMCs in Table 4 will be discussed in this section. Therefore, these parameters are calculated for specified subsets of

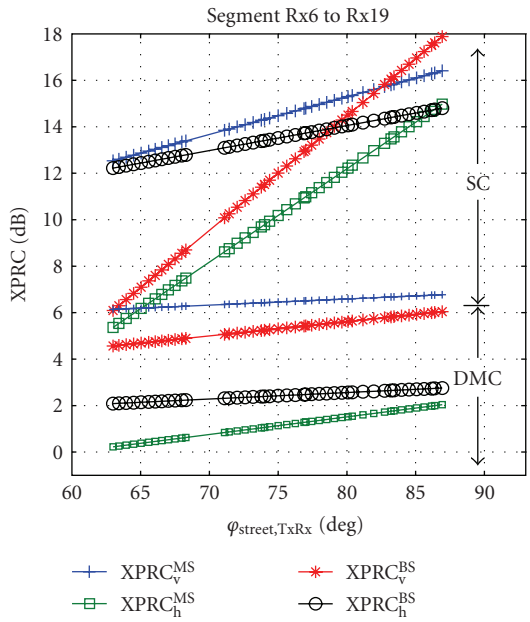

Figure 9: Change of the XPRCs dependent on the angle $\varphi_{\text{street,TxRx}}$.

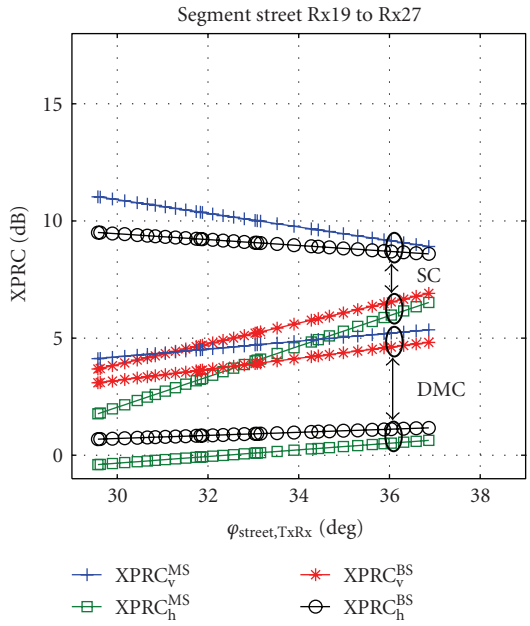

Figure 10: Change of the XPRCs dependent on the angle $\varphi_{\text{street,TxRx}}$, Rx19 to Rx27.

the whole measurement route. The subsets are classified into two groups: corners and streets. The conditions at each corner are quite different. The street subsets Rx1 to Rx6 (LOS), Rx19 to Rx27 (NLOS), and Rx38 to Rx6 (OLOS) are unique, whereas the streets Rx6 to Rx19 and Rx27 to Rx38 are comparable and consist of a mix of NLOS and OLOS measurements.

(i) All subsets under LOS condition have in common that the XPRC of the SCs for horizontal and vertical polarization are quite high. For the segments Rx1 to Rx6, the $\text{XPRC}_{\text{h}}^{\text{MS}}$ and $\text{XPRC}_{\text{v}}^{\text{BS}}$ are higher than $\text{XPRC}_{\text{v}}^{\text{MS}}$ and $\text{XPRC}_{\text{h}}^{\text{BS}}$, that is, the XPRCs of the channel are not equal at the BS and MS considering the same polarization. In the following, we will call a channel with this polarization behavior not symmetric, the symmetry being related mainly to the difference between the pathweights γ_{hv} and γ_{vh}. Exceptions in terms of the symmetry are the LOS measurements around corner Rx6. In this area, the channel seems to be symmetric with respect to the polarization.
The XPRC parameters of the DMC are in general 5 to 6 dB lower than the parameters of the SCs. At the MS side, the $\text{XPRC}_{\text{h}}^{\text{MS}}$ is around 3 dB lower than the $\text{XPRC}_{\text{v}}^{\text{MS}}$, and at the BS the XPRCs are almost equal for h and v.

(ii) The maximum XPRC values of the SCs in OLOS cases are 1 to 2 dB lower than in the LOS case. The gap between the DMC and the SC parameters is almost equal to the LOS cases. However, there is one significant difference: the SC and DMC parameters of the channel have almost the same properties at the BS and MS, that is, the two-by-two polarization matrix of the SC and DMC is symmetric. The four XPRCs of the SCs are almost equal, whereas in both cases (MS/BS) the XPRC_{v} values of the DMCs are around 3 to 5 dB higher than the XPRC_{h}s.

(iii) The measurement situations that are dominated by NLOS conditions are not symmetric in terms of the XPRC of the SCs. At the MS side, the vertical $\text{XPRC}_{\text{v}}^{\text{MS}}$ is higher, whereas, at the BS, the horizontal $\text{XPRC}_{\text{h}}^{\text{BS}}$ is higher, with $\text{XPRC}_{\text{h}}^{\text{MS}}$, respectively, $\text{XPRC}_{\text{v}}^{\text{BS}}$ being ca 5 dB lower. The cause of this can be found by analyzing the distribution of the four polarimetric pathweights. The cross-polarization values γ_{hv} have much higher values than the values of γ_{vh} and the copolar values γ_{hh} and γ_{vv} are almost equal.
For the DMCs, the vertical XPRCs are around 5 dB higher than the horizontal at the BS and MS sides.

In most cases, the $\text{PC}_{\text{v/h}}^{\text{MS}}$ of the SCs show that the received power having vertical polarization is higher (around $1, \ldots, 2$ dB). The LOS cases are the only exceptions (up to -4 dB). In the NLOS corners (around Rx19, Rx27), a slightly higher vertical power is received ($2, \ldots, 3$ dB). At the BS side, the variation of the $\text{PC}_{\text{v/h}}^{\text{BS}}$ is smaller ($-2, \ldots, 1$ dB) dependent on the subset.

Except for the corner Rx19 and the LOS street Rx1 to Rx6, the power ratio $\text{PC}_{\text{v/h}}$ of the DMCs is around 2 to 3 dB at the BS and MS.

From this statistical analysis, we can conclude that the polarization behavior of the SCs varies more with the local scattering situation (XPRC values between 3 dB and 15 dB) than that of the DMCs (XPRC values between 0 dB and 6 dB). The symmetry of the polarization matrix seems to have a strong relation to the measurement condition (LOS, OLOS, NLOS), which is summarized in Table 5. At the

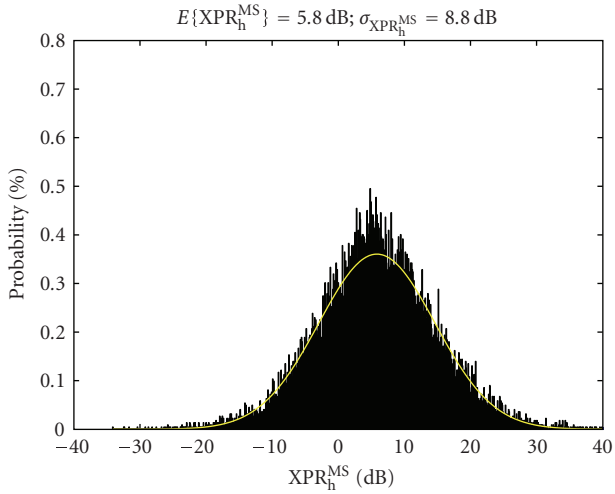

FIGURE 11: PDF of the $\mathrm{XPR}_{\mathrm{h}}^{\mathrm{MS}}$ of the SCs, macrocell Rx19 to Rx27.

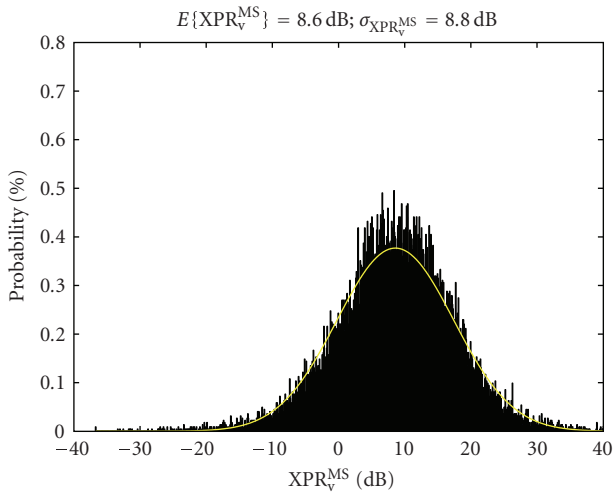

FIGURE 12: PDF of the $\mathrm{XPR}_{\mathrm{v}}^{\mathrm{MS}}$ of the SCs, macrocell Rx19 to Rx27.

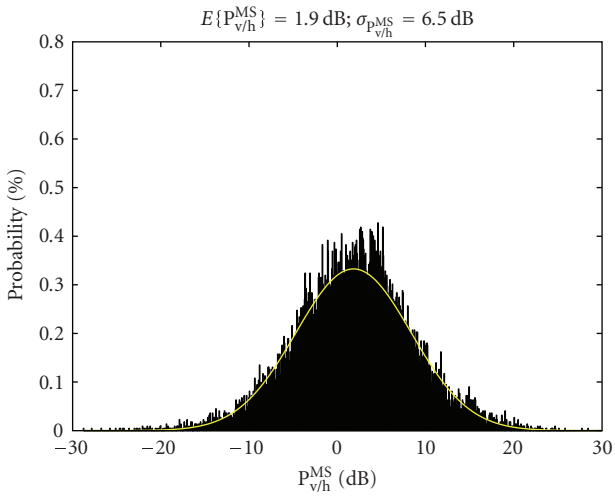

FIGURE 13: PDF of the $P_{\mathrm{v/h}}^{\mathrm{MS}}$ of the SCs, macrocell Rx19 to Rx27.

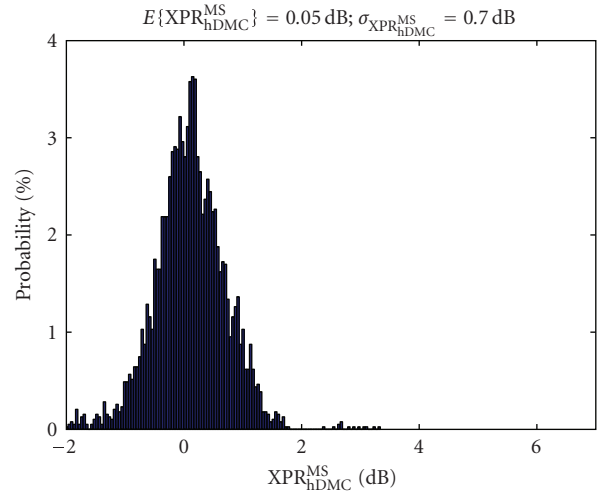

FIGURE 14: PDF of the $\mathrm{XPR}_{\mathrm{h}}^{\mathrm{MS}}$ of the DMCs, macrocell Rx19 to Rx27.

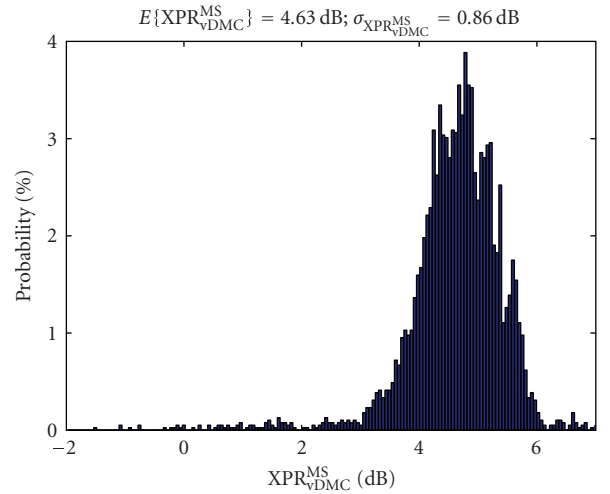

FIGURE 15: PDF of the $\mathrm{XPR}_{\mathrm{v}}^{\mathrm{MS}}$ of the DMCs, macrocell Rx19 to Rx27.

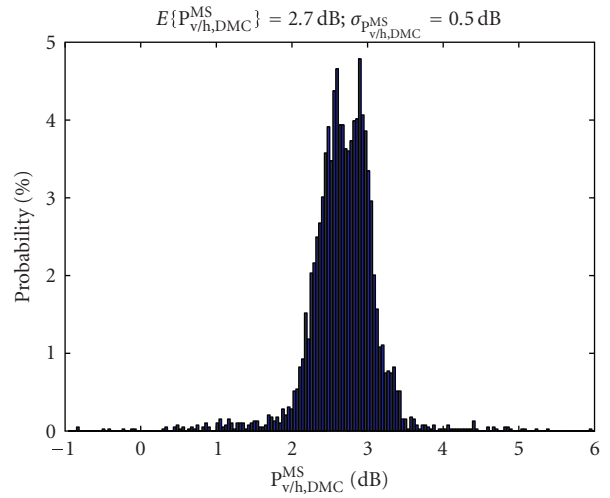

FIGURE 16: PDF of the $P_{\mathrm{v/h}}^{\mathrm{MS}}$ of the DMCs, macrocell Rx19 to Rx27.

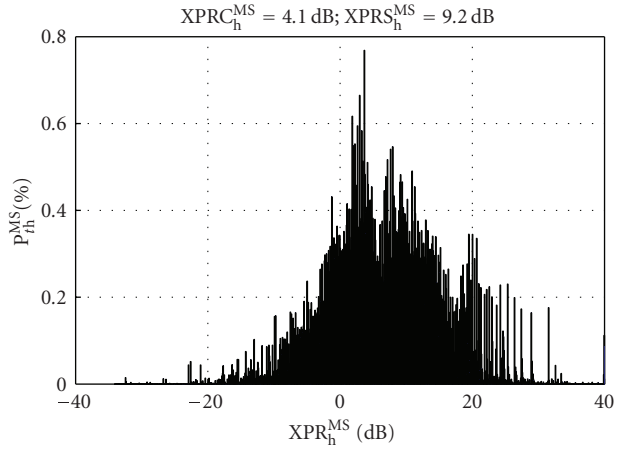

Figure 17: Normalized power distribution of P_{th}^{MS} dependent on the XPR_h^{MS} of the SCs, macrocell Rx19 to Rx27.

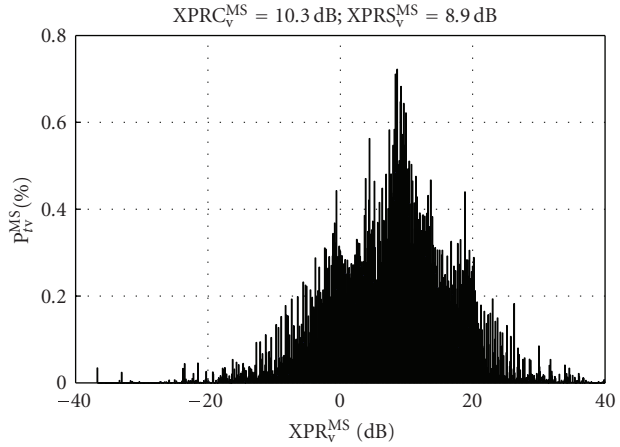

Figure 18: Normalized power distribution of P_{tv}^{MS} dependent on the XPR_v^{MS} of the SCs, macrocell Rx19 to Rx27.

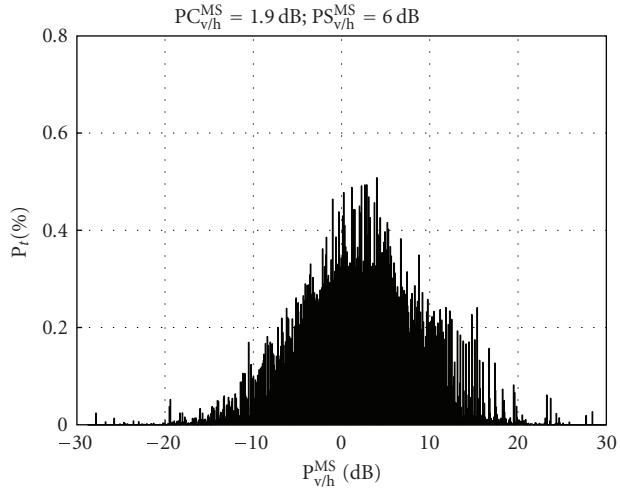

Figure 19: Normalized power distribution of P_t^{MS} dependent on $P_{v/h}^{MS}$ of the SCs, macrocell Rx19 to Rx27.

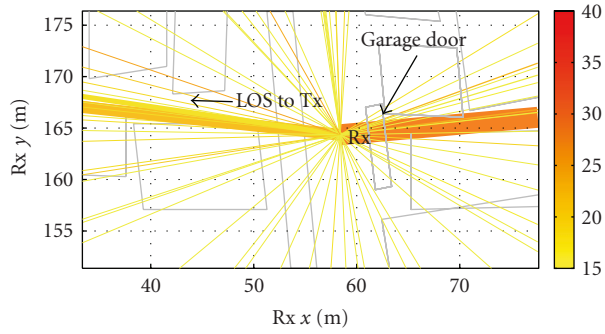

Figure 20: XPR_h^{MS} indicated by color, power $P_{h,k}^{MS}$ by linewidth.

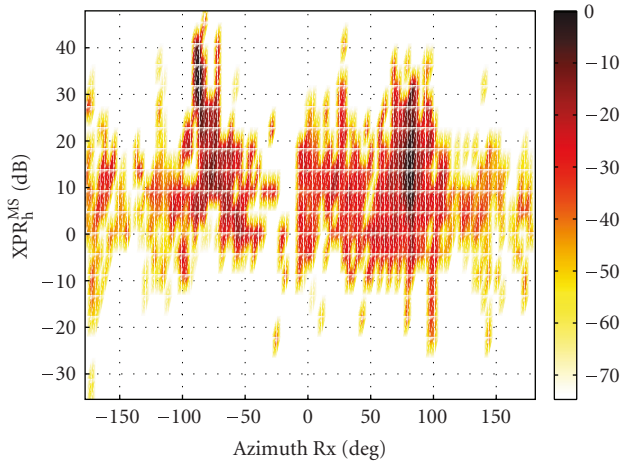

Figure 21: Power spectrum of P_{th}^{MS} dependent on Rx azimuth and XPR_h^{MS} of the SCs.

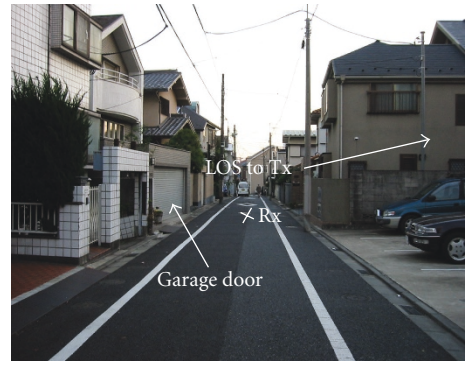

Figure 22: Environment around Rx.

MS side, the SCs are dominated by the vertical polarization, whereas at the BS, side the channel is dominated by horizontal polarization in terms of power ($PC_{v/h}$) and diversity (XPRC). This "general" behaviour is related to the higher number of NLOS measurement points. The DMCs are mainly dominated by the vertical polarization in terms of power ($PC_{v/h}$) and diversity (XPRC).

6.2. Local analysis

One could ask whether it is always sufficient to describe the measured scenario by statistical parameters that are derived from the analysis results of sets of measurement segments. The parameters XPRC of the SCs can strongly vary with the Rx position. Therefore, we calculated all parameters of XPRC and $PC_{v/h}$ of the SCs (Figures 23 to 28) and the DMCs (Figures 29 to 34) at each position within a snapshot interval $\Delta s = 20$, which covers a run length of ca 3 m.

Characteristics of the SCs

With respect to the XPRCs, the following were found.

(i) In the LOS region between Rx1 and Rx6, the XPRC values considering the whole segment are quite high (around 14 dB, see Table 3). From the local analysis, it is obvious that the $XPRC_v^{MS}$ and $XPRC_h^{BS}$ vary more (−3 dB to 20 dB) than the $XPRC_v^{BS}$ and $XPRC_h^{MS}$, which is mainly caused by the stronger change of the pathweights γ_{vh} than the change of the pathweights γ_{hv}. The behavior of the whole segment cannot be described by a known distribution.

(ii) Analyzing the position-dependent values of the segment Rx6 to Rx19, we can observe that all four XPRCs increase, while changing the Rx position from $y = 50$ m to $y = 200$ m. This behavior is related to the diffraction over rooftop and the strong single-bounce reflections on the opposite (in terms of Tx) side of the street, whereas the polarization vector is rotated dependent on the angle $\varphi_{\text{street,TxRx}}$ between the vector in the street direction and the vector between Tx and Rx. In the area Rx $y = 150$ m to $y = 200$ m, the incoming wave is almost perpendicular to the street Rx6 to Rx19. Due to this condition, the change of the polarization vector is smaller and the XPRC values are higher. Furthermore, the probability of OLOS condition is higher due to the layout of the residential area. In the area Rx $y = 50$ m to $y = 150$ m, the XPRC is lower since the street and the incoming wave are not perpendicular anymore, the polarization vector is changed. The change of the $XPRC_v^{BS}$ and $XPRC_h^{MS}$ moving from Rx $y = 50$ m to $y = 200$ m is bigger than the change of $XPRC_v^{MS}$ and $XPRC_h^{BS}$. The cause is probably the larger change in the horizontal polarization compared to the vertical, the pathweights γ_{hv} change more with angle $\varphi_{\text{street,TxRx}}$ than the pathweights γ_{vh}. For a better understanding of this phenomenon, we plotted the line fit of all XPRCs in Figure 9 and summarized the ΔXPRC and the standard deviation around the line fit in Table 6. The upper four curves in the figure are the values of the XPRCs of the SCs, whereas the lower four describe the DMCs.

(iii) For the segment between Rx27 and Rx38, we expect almost the same behavior like for the segments Rx6 to Rx19. The trend of the XPRCs seems to be the same but due to some positions with a quite irregular characteristics, it is impossible to approximate this segment with a line. One of these positions with an abnormal behavior will be discussed in Section 6.3.

(iv) The measurements in the segments Rx19 to Rx27 are mainly under NLOS condition. But, still, we can observe that the XPRCs dependent on the pathweights γ_{hv} vary quite strongly close to the corner Rx19. Analyzing each path dependent on the DoA and the XPR around the corner, it was observed that the paths coming from the far cluster 2 (next corner and some bigger buildings), which we mentioned in Section 4.1, have quite high XPR_v^{BS}s and XPR_h^{MS}s. Due to the cancelation of these paths while moving away from Rx19 in the direction of Rx27, the $XPRC_v^{BS}$ decreases around 10 dB. Besides, we note that the XPRCs dependent on γ_{vh} increase continuously while moving in the direction of Rx27. This behavior is shown in Figure 10 using the line fit dependent on the angle $\varphi_{\text{street,TxRx}}$, where the smaller angle is close to the corner Rx27 and the biggest is located around 10 m after the corner Rx19. In order to identify the SC and DMC correctly the respective curves are grouped (indicated by cycles in Figure 10). The 10 m interval after the corner is not used for the line fit due to the larger variation. After that distance, the XPRCs dependent on the γ_{hv} decrease in average while moving in the direction of Rx27, which is conform to an increase with angle $\varphi_{\text{street,TxRx}}$. This behavior is quite similar to that at the measurement positions of the segments Rx6 to Rx19 in the purely NLOS region. The ΔXPRCs are similar for these values (see Table 7).

(v) For the segments Rx38 to Rx6, almost all measurement points are under OLOS condition. The beginning and the end of this segment seem to follow a trend. But, on an interval in the middle of this segment, strong single-bounce scattering occurs at a building with a very smooth surface, as becomes apparent by analyzing the spatial-temporal parameters of the SCs. As the XPRCs change drastically, a line fit would be meaningless, at least for the parameters of the SCs.

With the contrast to the analysis of the XPRCs above, few clear relations can be found for the power ratio $PC_{v/h}$ between horizontal and vertical received (MS) or transmitted (BS). No strong relation to the angle $\varphi_{\text{street,TxRx}}$ was found. The ratios vary mainly with the local conditions around the Rx position.

Characteristics of the DMCs

With respect to the XPRCs, the following were found.

(i) For the XPRC of the DMCs (Figures 29 to 33), we can summarize that the development of these four values is quite similar. The $XPRC_v$s at the BS and at the MS are between 2 dB to 6 dB and around $2, \ldots, 3$ dB higher than $XPRC_h^{MS}$, $XPRC_h^{BS}$. Except for the LOS case the BS and MS parameters are similar, that is, the channel is symmetric in terms of polarization and the DMC.

Table 3: XPRC and XPRS of the SCs in dB.

Segment	MS side			BS side		
	$XPRC_h^{MS}$ [$XPRS_h^{MS}$]	$XPRC_v^{MS}$ [$XPRS_v^{MS}$]	$PC_{v/h}^{MS}$ [$PS_{v/h}^{MS}$]	$XPRC_h^{BS}$ [$XPRS_h^{BS}$]	$XPRC_v^{BS}$ [$XPRS_v^{BS}$]	$PC_{v/h}^{BS}$ [$PS_{v/h}^{BS}$]
Corner Rx6	14.9 [9.9]	12.6 [11.1]	−1.6 [5.6]	14.2 [10.6]	13 [9.6]	−1.1 [5.4]
Corner Rx19	3.5 [13.5]	11.2 [8.6]	3.1 [7.4]	9.2 [9.4]	5.7 [15.1]	−0.7 [9]
Corner Rx27	2.1 [7.8]	9.9 [8.9]	2.2 [5.6]	8.7 [8]	3.4 [10]	−1.5 [6.5]
Corner Rx38	10.1 [8.4]	12.6 [9.2]	1.2 [6.6]	11.7 [9.1]	11.3 [8.5]	0.7 [5.9]
Rx6 to Rx19	11.2 [9.4]	15.4 [8]	1.7 [5.2]	13.9 [8]	13.5 [11.5]	0.5 [6.8]
Rx19 to Rx27	4.1 [9.2]	10.4 [8.9]	1.9 [6]	9.1 [7.9]	6.1 [11.8]	−0.8 [6.6]
Rx27 to Rx38	11.9 [10.6]	14.7 [9.2]	1 [6]	14.3 [9.7]	13.1 [11.3]	0 [7.1]
Rx38 to Rx6	11.8 [8]	10.8 [9.5]	−0.3 [5.9]	10.1 [9.1]	12.6 [8.7]	0.3 [5.8]
Rx1 to Rx6	14.1 [8.5]	7.5 [13]	−4.1 [6.5]	10.5 [9.8]	11.3 [9.8]	−2 [5]

Table 4: XPRC and XPRS of the DMCs in dB.

Segment	MS side			BS side		
	$XPRC_h^{MS}$ [$XPRS_h^{MS}$]	$XPRC_v^{MS}$ [$XPRS_v^{MS}$]	$PC_{v/h}^{MS}$ [$PS_{v/h}^{MS}$]	$XPRC_h^{BS}$ [$XPRS_h^{BS}$]	$XPRC_v^{BS}$ [$XPRS_v^{BS}$]	$PC_{v/h}^{BS}$ [$PS_{v/h}^{BS}$]
Corner Rx6	2.5 [1.7]	6.9 [1.9]	1.6 [0.7]	5.5 [1.5]	4.1 [2.2]	0.2 [1.1]
Corner Rx19	−0.2 [1]	6.3 [1]	4.1 [0.6]	0.5 [1.7]	5.6 [0.9]	3.6 [0.8]
Corner Rx27	−0.6 [0.6]	4.6 [0.6]	2.8 [0.4]	0.9 [0.6]	3.3 [0.9]	1.8 [0.6]
Corner Rx38	0.4 [0.9]	5.5 [0.5]	2.9 [0.4]	1.9 [0.6]	4.2 [0.8]	2 [0.5]
Rx6 to Rx19	1.7 [1.7]	6.9 [1.6]	3.3 [1]	2.9 [1.5]	6.2 [2.6]	2.8 [1.4]
Rx19 to Rx27	0 [0.7]	4.7 [0.7]	2.6 [0.4]	1 [0.7]	3.8 [0.9]	2 [0.6]
Rx27 to Rx38	2.3 [2]	7.5 [2.1]	3 [0.8]	4 [2.5]	6 [1.7]	2.4 [0.9]
Rx38 to Rx6	0.9 [1.3]	5.9 [1.7]	2.8 [0.9]	2 [1]	4.9 [1.8]	2.2 [1]
Rx1 to Rx6	2.9 [1.2]	6.6 [1.2]	1.8 [0.5]	4.9 [1.3]	4.7 [1.3]	0.8 [0.6]

Table 5: Symmetry of the channel in terms of the polarization.

Condition	SC	DMC
LOS	Not symmetric	Not symmetric
NLOS	Not symmetric	Symmetric
OLOS	Symmetric	Symmetric

(ii) Furthermore, the values of the DMC are not varying so much compared to the SCs. The gradient, which expresses the dependence on the angle $\varphi_{\text{street,TxRx}}$, of all four XPRCs of the DMC in the pure NLOS regions is smaller than in the case of the SCs (Figures 9, 10, Tables 6, 7).

(iii) If the incoming wave is perpendicular to the street, the XPRC increases drastically (ca 3 dB), which is also related to the higher probability of OLOS due to the layout of the residential area (gaps parallel to the broadside direction of the Tx).

The $PC_{v/h}$ is between 2 and 4 dB, that is, the DMC power is mainly vertical. Furthermore, we can observe the same behavior at the BS side and the MS side, which again shows that the channel is symmetric for the DMCs in terms of the polarization.

Finally we would like to comment on the accuracy of the calculated values (15), since these results are based on measurements with a finite signal-to-noise ratio and limited resolution of the measurement system. Here, we briefly discuss the error of the $XPRC_h^{MS}$ and $XPRC_v^{MS}$ as an example. To use the equations of the error propagation, we need the derivatives of (15) with respect to real and imaginary parts of the two corresponding pathweights of all paths in the considered range Δs. Using the estimated variances of the corresponding pathweights (See Section 2), we have calculated the errors of the discussed parameters. As both derivations and resulting expressions are complex, we do not present them in this contribution.

Calculating these errors, we observed that the absolute error increases in areas with a high XPRC, where one of the pathweights is small. This means that the SNR is worse for

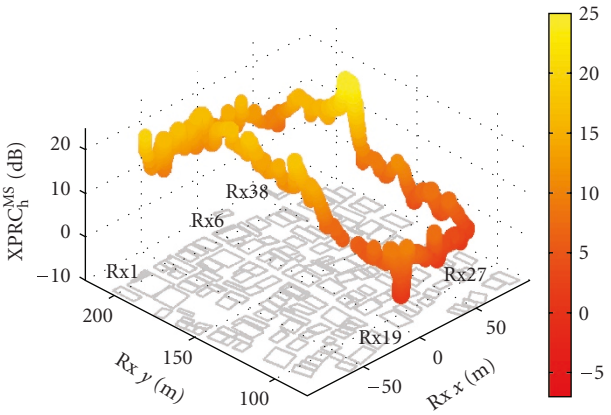

FIGURE 23: XPRC$_h^{MS}$ of the SCs $\Delta s = 20$ (ca 3 m).

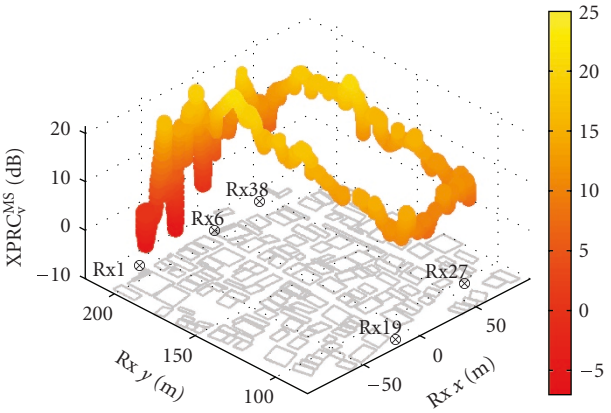

FIGURE 24: XPRC$_v^{MS}$ of the SCs $\Delta s = 20$ (ca 3 m).

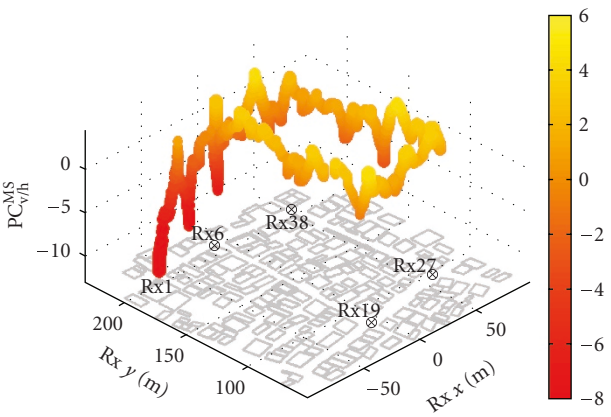

FIGURE 25: PC$_{v/h}^{MS}$ of the SCs $\Delta s = 20$ (ca 3 m).

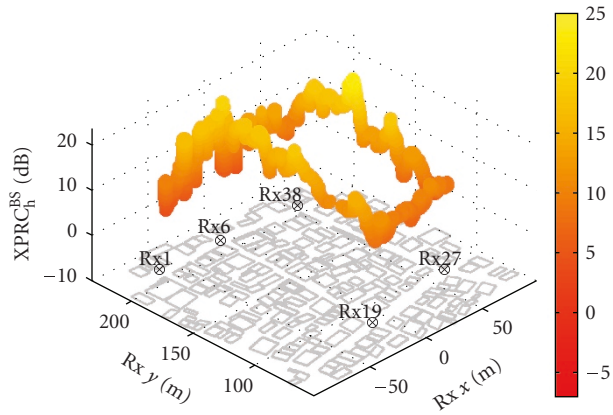

FIGURE 26: XPRC$_h^{BS}$ of the SCs $\Delta s = 20$ (ca 3 m).

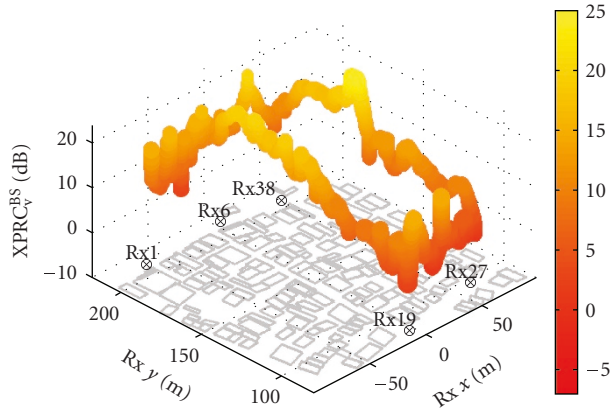

FIGURE 27: XPRC$_v^{BS}$ of the SCs $\Delta s = 20$ (ca 3 m).

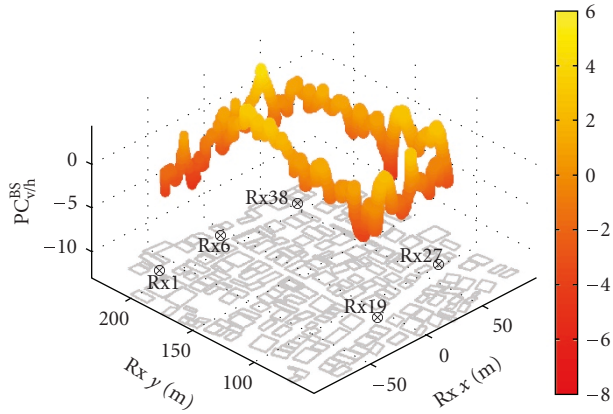

FIGURE 28: PC$_{v/h}^{BS}$ of the SCs $\Delta s = 20$ (ca 3 m).

these pathweights, resulting in higher variances. Therefore, we used the relative error, which is the ratio between the XPRC and the corresponding error. Around 75% of all positions have an XPRC$_v^{MS}$ (61% for XPRC$_h^{MS}$) with a relative error better than −10 dB. The difference between h and v can be explained by the lower total power in the h polarization especially in the NLOS cases, which causes higher variances of the estimated pathweigths. The remaining 25% (39% for XPRC$_h^{MS}$) of the values have an error worse than −10 dB. In these cases with larger errors, closely spaced paths could be observed. As the resolution and the SNR are limited, the variance of the parameters increases.

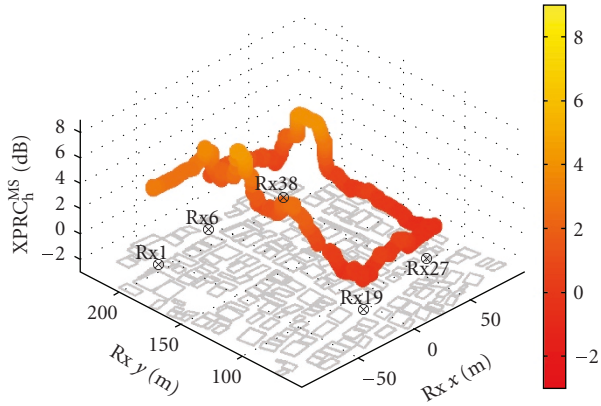

Figure 29: XPRC$_h^{MS}$ of the DMCs $\Delta s = 20$ (ca 3 m).

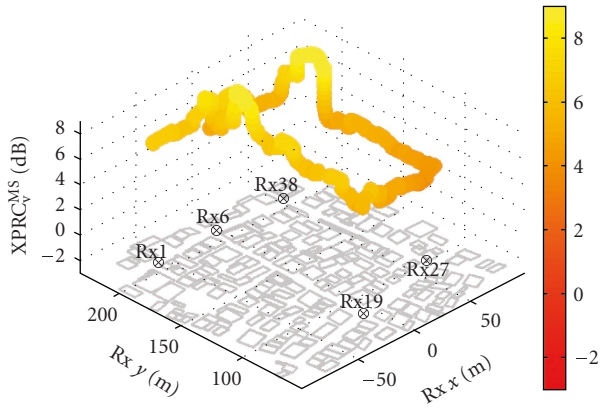

Figure 30: XPRC$_v^{MS}$ of the DMCs $\Delta s = 20$ (ca 3 m).

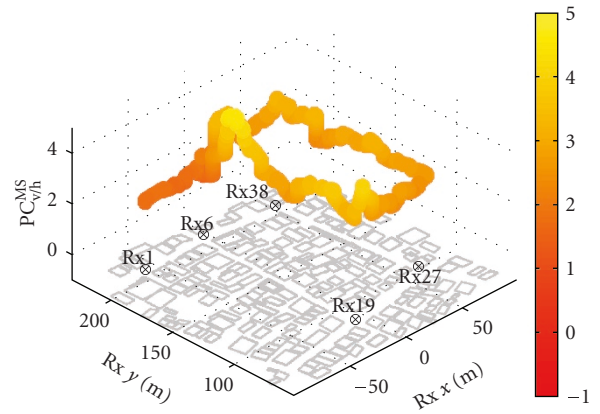

Figure 31: PC$_{v/h}^{MS}$ of the DMCs $\Delta s = 20$ (ca 3 m).

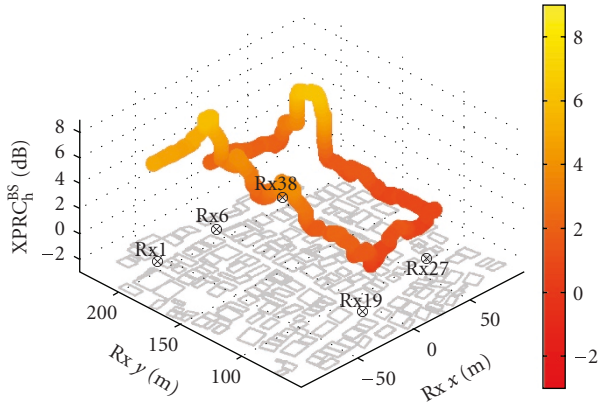

Figure 32: XPRC$_h^{BS}$ of the DMCs $\Delta s = 20$ (ca 3 m).

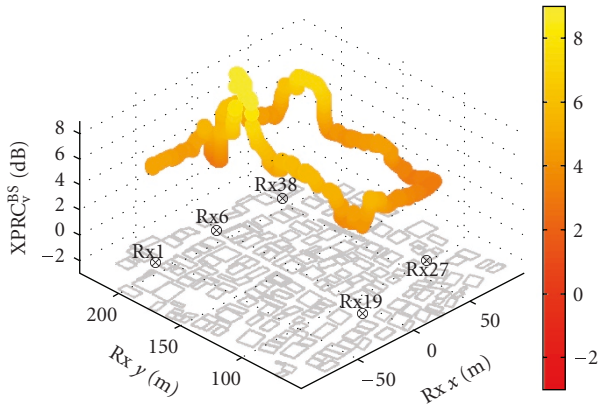

Figure 33: XPRC$_v^{BS}$ of the DMCs $\Delta s = 20$ (ca 3 m).

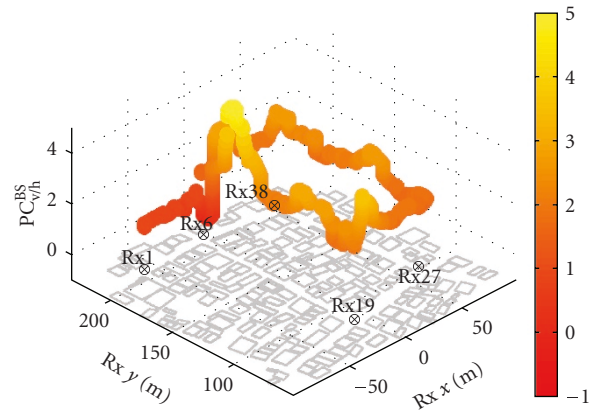

Figure 34: PC$_{v/h}^{BS}$ of the DMCs $\Delta s = 20$ (ca 3 m).

6.3. *Measurement positions with a specific behavior*

In the previous section, we discussed general trends in the analyzed measurement data in terms of the polarization. Nevertheless, in certain measurement intervals no such trends were observed. Yet, we noted an increased total specular power at positions with a specific behavior. In the following, we will discuss one of these positions where we observe a quite different behavior compared to the surrounding area.

Around the Rx position $x = 60$ m, $y = 165$ m on the street Rx27 to Rx38, the values of the XPRC$_h^{MS}$, XPRC$_h^{BS}$, and XPRC$_v^{BS}$ of the SCs increase drastically (see Figures 23, 26, 27). The values vary between 20 dB and 22 dB, which

Table 6: ΔXPRC segments Rx6 to Rx19.

	Parameter	Standard deviation from the polynom fit (dB)	ΔXPRC (dB/deg)
SC	$XPRC_v^{MS}$	1.2	0.2
	$XPRC_h^{MS}$	2.2	0.4
	$XPRC_v^{BS}$	1.8	0.5
	$XPRC_h^{BS}$	1.8	0.1
DMC	$XPRC_v^{MS}$	0.6	0.03
	$XPRC_h^{MS}$	0.7	0.07
	$XPRC_v^{BS}$	0.7	0.06
	$XPRC_h^{BS}$	0.8	0.03

Table 7: ΔXPRC segments Rx19 to Rx27.

	Parameter	Standard deviation from the polynom fit (dB)	ΔXPRC (dB/deg)
SC	$XPRC_v^{MS}$	1	−0.3
	$XPRC_h^{MS}$	1.2	0.7
	$XPRC_v^{BS}$	3.2	0.4
	$XPRC_h^{BS}$	1.2	−0.1
DMC	$XPRC_v^{MS}$	0.3	0.2
	$XPRC_h^{MS}$	0.3	0.1
	$XPRC_v^{BS}$	0.2	0.2
	$XPRC_h^{BS}$	0.4	0.1

is relatively high for the measurement scenario except for LOS positions. To identify the source of these high XPRC values, the estimated DoAs are used. In Figure 20, the estimated paths are plotted in the environment around the mentioned position. The color of the rays indicate the XPR_h^{MS} and the line width indicates the strength in terms of $P_{h,k}^{MS}$. The characteristics of the values XPR_h^{BS} and XPR_v^{BS} are similar to XPR_h^{MS}. The zero direction in azimuth of the Rx antenna array is pointing to the north of the map, where we count the azimuth angle counterclockwise.

In the area between −70° and −90° azimuth, the XPR_h^{MS} is around 40 dB (see Figure 21). The cause of this behavior is the metallic garage door (Figure 22). The measurements are still taken under NLOS conditions but we receive a very strong single bounce from that door. Furthermore, we can observe a quite high XPR_h^{MS} (ca 30 dB) around the corner of the building at the right side of the street in the direction of 70° azimuth. The reason here is the diffraction of LOS around the edge of the building. All other scatterers in the direction of the street or the street corners have a much lower XPR_h^{MS} (around 10 dB). These values are comparable to XPR_h^{MS} values of the adjacent measurement positions that do not show this specific behavior. The parameters of the DMC are almost constant in this and the adjacent area.

The described position is not the only position with a unusual behavior. Along the entire measurement route, several positions could be found. The cause of the specific behavior, for example large smooth building surfaces, metallic objects, and far clusters, could be mostly identified by using the estimated directional parameters. Currently, we are analyzing other scenarios where we observe similar effects.

7. CONCLUSIONS

We have introduced different parameters characterizing the polarization behavior of the channel. From macrocell measurements, we have shown that the XPRs are lognormal distributed. We have highlighted the importance of power-weighted XPR.

Two different approaches to analyze the measurement data were taken. On one hand, we analyzed statistical parameters over sets of segments of the measurement. On the other hand, we made a local analysis. We demonstrated that in both cases, the symmetry of the polarization matrix is strongly dependent on measurement conditions like LOS, OLOS, and NLOS. Certain trends can be deduced from analyzes of sets of segments. From local analyzes, two effects became apparent. The change of the polarization vector of the specular components and the diffuse scattering can be related to the angle between the street and the direct connection between the transmitter and receiver. It was shown that the polarization parameters of the specular components show more variations than those of the diffuse scattering. Some measurement positions with a specific behavior, that is, with strongly varying polarization parameters, are discussed. Plausible causes for these variations could be identified: metallic objects, large smooth building surfaces, and far clusters. In this macrocell environment, we observed that such objects can significantly change the polarization behavior in an area. Neither with global nor with local analyzes, the power-weighted XPR resembles a known distribution.

ACKNOWLEDGMENTS

This research is partly supported by the National Institute of Information and Communications Technology of Japan. Furthermore, we would like to thank the members of Takada Laboratory for the support during measurements.

REFERENCES

[1] C. Oestges, V. Erceg, and A. J. Paulraj, "Propagation modeling of MIMO multipolarized fixed wireless channels," *IEEE Transactions on Vehicular Technology*, vol. 53, no. 3, pp. 644–654, 2004.

[2] L. Dong, H. Choo, R. W. Heath Jr., and H. Ling, "Simulation of MIMO channel capacity with antenna polarization diversity," *IEEE Transactions on Wireless Communications*, vol. 4, no. 4, pp. 1869–1872, 2005.

[3] J. Hämäläinen, R. Wichman, J.-P. Nuutinen, J. Ylitalo, and T. Jämsä, "Analysis and measurements for indoor polarization MIMO in 5.25 GHz band," in *Proceedings of 61st IEEE Vehicular Technology Conference (VTC '05)*, vol. 1, pp. 252–256, Stockholm, Sweden, May-June 2005.

[4] C. Waldschmidt, C. Kuhnert, T. Fügen, and W. Wiesbeck, "Measurements and simulations of compact MIMO-systems based on polarization diversity," in *Proceedings of IEEE Topical Conference on Wireless Communication Technology*, pp. 284–285, Honolulu, Hawaii, USA, October 2003.

[5] P. Goud Jr., C. Schlegel, W. A. Krzymień, et al., "Indoor MIMO channel measurements using dual polarized patch antennas," in *Proceedings of IEEE Pacific RIM Conference on Communications, Computers, and Signal Processing (PACRIM '03)*, vol. 2, pp. 752–755, Victoria, BC, Canada, August 2003.

[6] P. Kyritsi, D. C. Cox, R. A. Valenzuela, and P. W. Wolniansky, "Effect of antenna polarization on the capacity of a multiple element system in an indoor environment," *IEEE Journal on Selected Areas in Communications*, vol. 20, no. 6, pp. 1227–1239, 2002.

[7] R. Thomä, D. Hampicke, M. Landmann, A. Richter, and G. Sommerkorn, "Measurement-based parametric channel modelling (MBPCM)," in *Proceedings of International Conference on Electromagnetics in Advanced Applications (ICEAA '03)*, Torino, Italy, September 2003.

[8] M. Haardt, R. Thomä, and A. Richter, "Multidimensional high-resolution parameter estimation with applications to channel sounding," in *High-Resolution and Robust Signal Processing*, Y. Hua, A. B. Gershman, and Q. Cheng, Eds., pp. 253–337, Marcel Dekker, New York, NY, USA, 2003.

[9] B. H. Fleury, M. Tschudin, R. Heddergott, D. Dahlhaus, and K. I. Pedersen, "Channel parameter estimation in mobile radio environments using the SAGE algorithm," *IEEE Journal on Selected Areas in Communications*, vol. 17, no. 3, pp. 434–450, 1999.

[10] A. Richter, *On the estimation of radio channel parameters: models and algorithms (RIMAX)*, Ph.D. thesis, Technische Universität Ilmenau, Ilmenau, Germany, 2005.

[11] M. Landmann and R. Thomä, "Estimation of phase drift during calibration measurements for efficient beam pattern modelling," in *Proceedings of NEWCOM-ACoRN Workshop*, Vienna, Austria, September 2006.

[12] J. Medbo, M. Riback, H. Asplund, and J. Berg, "MIMO channel characteristics in a small macrocell measured at 5.25 GHz and 200 MHz bandwidth," in *Proceedings of the 62nd IEEE Vehicular Technology Conference (VTC '05)*, vol. 1, pp. 372–376, Dallas, Tex, USA, September 2005.

[13] X. Yin, B. H. Fleury, P. Jourdan, and A. Stucki, "Polarization estimation of individual propagation paths using the SAGE algorithm," in *Proceedings of 14th IEEE International Symposium on Personal, Indoor and Mobile Radio Communications (PIMRC '03)*, vol. 2, pp. 1795–1799, Beijing, China, September 2003.

[14] G. S. Ching, M. Ghoraishi, N. Lertsirisopon, et al., "Wideband directional radio propagation channel analysis inside an arched tunnel," in *Proceedings of the 17th International Symposium on Personal, Indoor and Mobile Communications (PIMRC '06)*, Helsinki, Finland, September 2006.

[15] L. M. Correia, *Mobile Broadband Multimedia Networks: Techniques, Models and Tools for 4G*, Elsevier, London, UK, 2006.

[16] IST-4-027756 WINNER II D1.1.1 Interim report, "WINNER II interim channel models," https://www.ist-winner.org.

[17] R. Thomä, M. Landmann, A. Richter, and U. Trautwein, "Multidimensional high-resolution channel sounding measurement," in *Smart Antennas—State of the Art*, T. Kaiser, A. Bourdoux, H. Boche, J. R. Fonollosa, J. B. Andersen, and W. Utschick, Eds., vol. 3 of *EURASIP Book Series on Signal Processing and Communications*, pp. 241–270, Hindawi, New York, NY, USA, 2005.

[18] http://www.channelsounder.de.

[19] K. Kalliola, K. Sulonen, H. Laitinen, O. Kivekäs, J. Krogerus, and P. Vainikainen, "Angular power distribution and mean effective gain of mobile antenna in different propagation environments," *IEEE Transactions on Vehicular Technology*, vol. 51, no. 5, pp. 823–838, 2002.

[20] J. B. Andersen, J. Ø. Nielsen, G. Bauch, and M. Herdin, "The large office environment - measurement and modeling of the wideband radio channel," in *Proceedings of the 17th Annual IEEE International Symposium on Personal Indoor and Mobile Radio Communications (PIMRC '06)*, Helsinki, Finland, September 2006.

[21] http://www.irk-dresden.de.

[22] K. Sivasondhivat, M. Landmann, J.-i. Takada, Y. Nakaya, I. Ida, and Y. Oishi, "Full polarimetric 3-D double directional channel measurement in a NLOS macrocellular environment," Tech. Rep. AP2005-117, IEICE, Tokyo, Japan, 2005.

[23] A. Kainulainen, L. Vuokko, and P. Vainikainen, "Polarization behaviour in different urban radio environments at 5.3 GHz," COST 273 Temporary Document TD(05)018, Bologna, Italy, 2005.

[24] L. Vuokko, P. Vainikainen, and J.-i. Takada, "Clusters extracted from measured propagation channels in macrocellular environments," *IEEE Transactions on Antennas and Propagation*, vol. 53, no. 12, pp. 4089–4098, 2005.